A New Method for Ionospheric Tomography and its Assessment by Ionosonde electron density GPS TEC and single-frequency PPP

Fabricio dos Santos Prol[1,2], Paulo de Oliveira Camargo[1], Manuel Hernández-Pajares[2], and Marcio Tadeu de Assis Honorato Muella[3]

[1]Universidade Estadual Paulista – UNESP - Roberto Simonsen, 305, Presidente Prudente, São Paulo, Brazil, 19060-900

[2]UPC-IonSAT, Barcelona, Spain

[3]Universidade do Vale do Paraíba – UNIVAP - Laboratório de Física e Astronomia, IP&D, São José dos Campos, São Paulo, Brazil, 12244-000

F. S. Prol, e-mail: fabricioprol@hotmail.com;

P. O. Camargo, e-mail: paulo@fct.unesp.br;

M. Hernández-Pajarez, e-mail: manuel.hernandez@upc.edu

M. T. A. H. Muella, e-mail: mmuella@univap.br.

Abstract A new tomographic method was developed with the main goal of mapping the ionosphere in the Brazilian region. The ionospheric background was estimated based on ionosonde and radio-occultation measurements to overcome the lack of data of climatological models in low-latitude regions. A new way of performing iterations of the conventional Multiplicative Algebraic Reconstruction Technique (MART) was also used in order to avoid non-illuminated cells and improve the spatial resolution. The quality assessment using independent ionosonde data during two weeks during 2013 showed a better performance of the proposed method in comparison to the International Reference Ionosphere, providing an improvement of 31% for the F-layer peak height and 24% for the ionospheric peak of electron density . The tomographic technique was also evaluated in the estimation of the Total Electron Content (TEC) and in the single-frequency Precise Point Positioning (PPP). An improvement of 59% in TEC and 31% in the single-frequency PPP was obtained in comparison to the results derived from Global Ionospheric Maps. In addition, a better daily description of the ionosphere was obtained with the proposed method, where it was possible

to detect the strong elevations of the peak height associated to the pre-reversal enhancement of the vertical plasma drift that occurs near sunset hours. The results reveal that the modified form of the MART tomographic technique can be considered a useful tool to technical and scientific communities involved in Space Weather, Spatial Geodesy and Telecommunications.

Keywords MART, GNSS, EIA, 3D Ionosphere, pre-reversal enhancement **E**x**B** drift, Radio-Occultation.

Introduction

Ionospheric tomography systems have been extensively used in the last decades to retrieve valuable information of the electron density distributions (Austen et al. 1988; Raymund et al. 1994; Pryse et al. 1998; Howe et al. 1998; Hernandez Pajares et al., 1998; Mitchell and Spencer 2003; Bust and Mitchell 2008; Kunitsyn et al. 2011; Prol et al. 2017). Despite considerable progress of the tomographic algorithms in the last years (Wen et al. 2012; Yao et al. 2013; Seemala et al. 2014; Zheng et al. 2015; She et al. 2017; Ghaffari Razin and Voosoghi 2017; Yin et al. 2017), the accuracy of the three-dimensional (3D) ionosphere reconstruction still presents a continuous challenge for many applications. One of the main issues is the description of certain particularities of the actual ionosphere at the most challenging conditions of the tropical region (Prol et al. 2016). The peculiarities of the ionosphere at tropical latitudes are characterized by the presence of several ionospheric events, such as plasma bubbles (Ely et al. 2012; Haase et al. 2011), Equatorial Ionization Anomaly (EIA) (Tulasi Ram et al. 2009; Materassi and Mitchell 2005), layered structures, for instance the sporadic E-layer (Zhao et al. 2011; Batista et al. 2008; Rishbeth 2000), and strong vertical drifts upwards during the evening pre-reversal enhancement (Batista et al. 1996; Abdu et al. 2008). Consequently, ionospheric tomography methods, specially

developed to describe the tropical region, may contribute to many studies related to the ionospheric dynamics and morphology.

Despite the relevance of better understanding the physical processes of the electron density distributions, the ionosphere still remains as a significant obstacle to the accuracy of the Global Navigation Satellite Systems (GNSS) positioning in the single-frequency Precise Point Positioning (PPP). The ionospheric models developed to improve the GNSS positioning in the Brazilian longitudinal sector, the region analyzed in this work, were based on two-dimensional representations of the Vertical Total Electron Content (VTEC) (Camargo et al., 2000; Aguiar and Camargo, 2012; Machado and Fonseca Jr, 2013). However, unavoidable errors degrade the GNSS positioning using these models due to the approximation of the ionosphere as a thin shell with constant height. In order to mitigate such errors, the ionospheric tomography allows performing the estimation of the ionospheric delay considering the ionosphere as a set of layers. Therefore, the ionospheric tomography might improve the traditional GNSS positioning due the possibility of estimating the ionospheric delay without the need of using an unrealistic mapping function to convert VTEC into the slant direction.

Previous works have already used tomographic reconstruction methods to map the ionosphere at the Brazilian region. For instance, Muella et al. (2011), used the four-dimension Multi Instrument Data Analysis System (MIDAS) algorithm to analyze the seasonal and hourly accuracy of the F2-layer peak density ( ) in the maximum period of the solar cycle 23. Also, Prol et al. (2016) have checked the accuracy of the Multiplicative Algebraic Reconstruction Technique (MART) to the estimation of and the Total Electron Content (TEC) during the maximum of the solar cycle 24. However, according to the authors the lack of data due to an inappropriate geometrical coverage can be considered to have a major impact in the accuracy of tomographic reconstruction. In order to overcome part of the

problem, this work presents a tomography algorithm specially developed considering the real scenario of data for the Brazilian tropical region. In addition, a pioneering analysis is presented to check the accuracy of the ionospheric tomography results to correct the ionospheric delay in the single-frequency PPP and the estimation of the peak height ( ).

Two main points have been considered in the development of the proposed method. Firstly, the algorithm should represent relatively small structures in order to detect high ionospheric variabilities. Secondly, the formulation should consider the lack of data derived from GNSS stations over Brazil, which had about 100 GNSS stations to cover the entire region during the year 2013. Indeed, the lack of data in the Brazilian region discards the possibility of using the most prominent constrained tomographic algorithms (Seemala et al. 2014), which requires a large dataset. It seems, therefore, reasonable to apply tomographic algorithms based on a priori information of the ionosphere, i.e., a background model. This is usually retrieved from climatological models, such as the International Reference Ionosphere (IRI) (Bilitza et al. 2014). However, due the lack of data in low-latitude regions, such climatological models usually do not describe certain particularities of the actual ionosphere in the most challenging equatorial conditions. In this respect, a new way to generate the ionospheric background has been developed by including actual data in the equatorial region. The new background formulation is based on Ionosonde and Radio-Occultation (RO) measurements, which gave us a well distributed global coverage of the ionosphere.

With the impulse of the results obtained by Prol et al. (2016), the MART technique has been chosen to update the background in a tomographic reconstruction of the Brazilian area. Indeed, Prol et al. (2016) applied the conventional MART with a low spatial resolution of 4° x 4° in latitude by longitude, which avoided issues of many non-illuminated cells. However, this is a low resolution for representing the ionospheric variability in the Brazilian region. In order to use a spatial resolution that was enough for showing small structures and,

at the same time, avoid non-illuminated cells, we also included VTEC observations. Therefore, a slight different method than the conventional MART has been developed, which enabled to take the maximum advantage of the GNSS observations available in the region. The next sections show the developed formulation in details. Also, the following section shows result and discussions of the method when assessed in terms of the peak height, the electron density peak, TEC and single-frequency PPP. Then, we present the conclusions about the new method as applied to the Brazilian region.

Ionospheric Background

The main goal of the ionospheric background in this work is to give an initial guess of the actual ionosphere with reasonable performance in the estimation of the shape of the ionospheric profiles, peak height and electron density at the peak. In this respect, the ionospheric profile measured by RO techniques and ionosondes were used to retrieve six parameters that define the ionospheric background. For the ionospheric peak, were obtained the peak height and the peak electron density ; for the topside, the two parameters were the scale height at a reference height (e.g. at the peak) and its gradient ; and for the bottomside ionosphere, were obtained the thickness parameter and scale factor .

The topside of the ionospheric background was estimated using the following equations that describes a linear Vary-Chap function:

with

where stands to the electron density at the height and is the varying scale height. The scale height and its gradient were estimated with a linearized Least Square fitting of Eq. (1), linked to Eq. (2) and using all electron density observations above .

The bottomside was estimated based on the formulation proposed by Ramakrishnan and Rawer (1972) and implemented in IRI, which is given by the following equations:

_____

with

_____

where measurements of were used to retrieve and parameters by a linearized Least Square fitting procedure. Despite the F1, E and D layers are important in describing several dynamics of the ionosphere, they were neglected in the background estimation due to their comparative lower electron densities. At lower heights the accuracy of the RO is reduced and, therefore, only the F2 layer was considered for the representation of the bottomside.

After applying the estimation procedure given by the fitting of Eqs. (1) and (3) for each ionospheric profile, the values of , , , , and were recorded with the horizontal position related to the coordinates of the peak height. In order to process the spatial interpolation of them and obtain global maps of the background at a given day, ionosonde measurements obtained in one day coupled with 60 days of data retrieved from RO were superimposed in a sun-fixed reference frame. Figure 1 (top) shows the location of the ionosonde stations, where data derived from the Space Physics Interactive Data Resource (SPIDR) were automatically processed and the data obtained by the Instituto Nacional de Pesquisas Espaciais (INPE) were manually retrieved. The INPE ionosondes are located in Brazil and corresponds to São Luís (SAA0K: 2.3°S, 44°W; magnetic lat. 0.8°S), Boa Vista (BVJ03: 2.8°N, 60.7°W; magnetic lat. 12.9°N) and Fortaleza (FZA0M: 3.8°S, 38.0°W; magnetic lat. 5.5°S). Also, Figure 1 (bottom) shows the spatial distribution superimposed with 60 consecutive days of RO data in terms of Local Time (LT) and magnetic latitude. The RO ionospheric profiles were derived from the FORMOSA Satellite Series No.

151 3/Constellation Observing System for Meteorology, Ionosphere, and Climate (FORMOSAT-
152 3/COSMIC) and processed by the University Corporation for Atmospheric Research
153 (UCAR). The location of each estimated is represented by one point in the map and
154 converted in the critical frequency by .
155

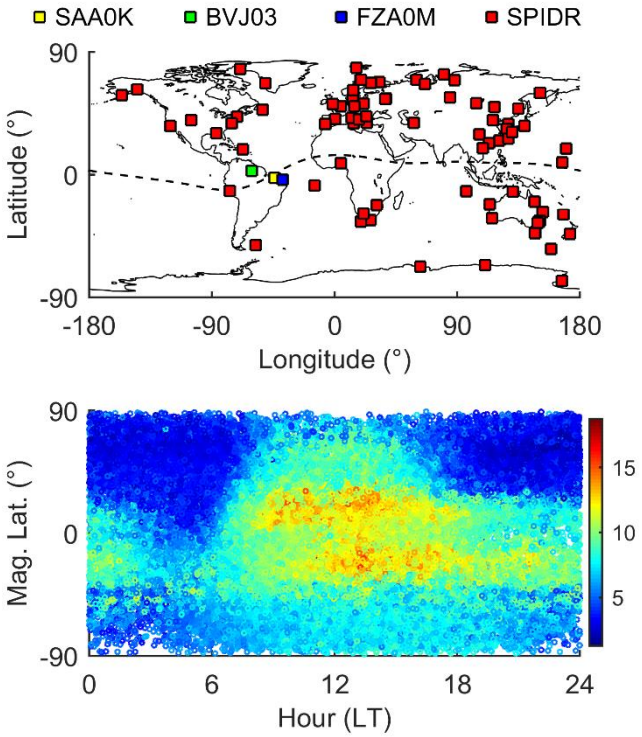

156

157 **Fig. 1** Location of the ionosonde stations of the global network of SPIDR and from the
158 regional network of INPE (top panel) and 60 superimposed days of data derived from
159 the COSMIC Data Analysis and Archive Center (CDAAC) (bottom panel) with the central
160 day in DOY (Day Of Year) 312 of 2013. The unit of the color bar is MHz.
161

162 Given the values of , , , , and in LT and magnetic latitude, a
163 spatial interpolation was performed. Figure 2 shows an example of the estimated spatial
164 distributions during DOY 312 of 2013 when applying a linear interpolation. RO and
165 ionosonde measurements were used together for the estimation of , and only RO data

was used for the estimation of , , and . As can be seen, the estimated values show the expected global patterns of , such as a clear daily variation and the representation of the two crests associated with the Equatorial Ionization Anomaly (EIA). Also, the estimated distributions are higher in the equatorial region due to the electron density distribution driven by the resulting force of the electric and geomagnetic fields in the ionosphere. In addition, the spatial distributions of and were estimated with similar behavior than reported in previous works (e.g., Olivares-Pulido et al., 2016, Hernández-Pajares et al. 2017). It is noticed here at the equatorial region a spatial anticorrelation between 30 km and 100 km for and -0.1 and 0.1 for . In the case of the bottomside, no previous work has calculated and values with the RO ionospheric profiles to compare with the obtained distributions. However, as can be seen in the bottom panels, the magnitude and spatial distribution of and seems reliable when comparing to the representations obtained from the International Reference Ionosphere 2012 (IRI-2012).

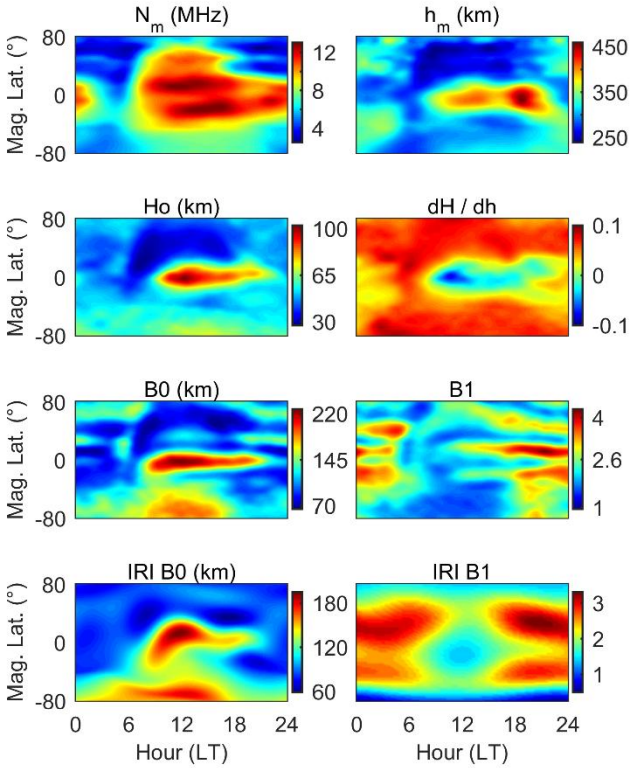

Fig. 2 Global estimation of , , , and to be used to generate a background for the ionospheric tomography in DOY 312 of 2013. The bottom panels show the and distributions computed with IRI-2012.

Once calculated the distributions of , , , , and in the sun-fixed reference frame, the global maps were converted in an earth-fixed reference frame in the regional area of Brazil. In this direction, the magnetic latitudes have been converted into geographical latitudes and the LT maps were projected along with the geomagnetic lines to create a set of maps in Universal Time (UT). Therefore, it was possible to obtain regional maps of , , , , and for a specific time and then to calculate the electron density at any height in the Brazilian region to be used as background for the regional tomography.

Regional Tomography

The main goal of the regional tomography in this work was to update the ionospheric background using TEC measurements of regional GNSS networks. The regional stations used to obtain TEC observations were selected from GNSS networks of IGS, RBMC (Rede Brasileira de Monitoramento Contínuo), LISN (Low-latitude Ionospheric Sensor Network), RAMSAC (Red Argentina de Monitoreo Satelital Continuo) and CALIBRA (Countering GNSS High accuracy Applications Limitations due to Ionospheric Disturbances in Brazil). The location of the GNSS stations is presented in the left panel of Figure 3. Also, the right panel shows the stations used for the evaluation of the regional tomography, where none of these stations were used in the tomographic reconstruction, i.e., they provided independent reference data. It is important to mention that the independent stations were selected in order to cover the most active ionosphere in the Brazilian region, i.e., the south crest of EIA.

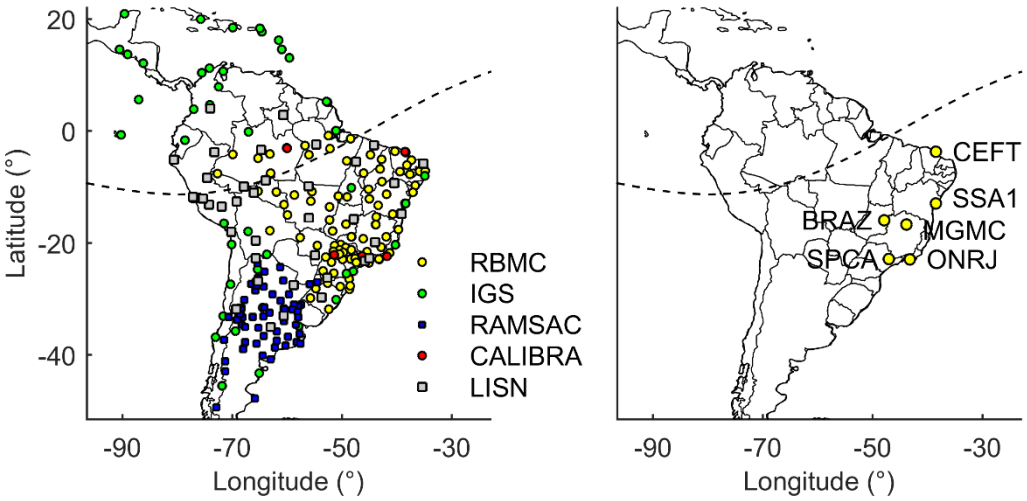

Fig. 3 Location of the GNSS stations used in the tomography (left panel) and GNSS station used in the assessment with independent data (right panel). The dashed line represents the magnetic equator.

The ionospheric information derived from GNSS measurements was obtained using a calibration method. A bias term over one arc of data with no cycle slips was first estimated by the weighting mean difference of the GNSS carrier phase measurements minus the TEC retrieved by Global Ionospheric Maps (GIMs), as:

with

where is the frequency (Hz) of the carrier, is the wavelength (m) in L1 and L2, is the carrier phase measurement of GPS (in cycles), is the bias term (m), is an elevation dependent weighting parameter for each and is the number of observations in an arc with continuous data. information is derived from the UQRG GIMs produced by Universitat Politècnica de Catalunya (UPC, see Hernández-Pajares, 1999), presently one of the bests or the best behaving IGS GIM (see Roma-Dollase et al. 2017). Also, the weighting parameter is based on the standard deviation of TEC derived from the root mean square maps available in GIM files, such as used by Prol et al. (2018).

Once calculated the bias for all the continuous arcs, TEC in a single epoch was directly calculated using the following equation:

where only arcs with a minimum of 5 minutes of continuous data and with a cut-off angle of 10° were used.

In addition to the TEC measurements, VTEC observations were included in the regional tomography. The VTEC observations were derived by applying the standard mapping function to convert the observed TEC using Eq. (7) into VTEC with the following equation:

where is the zenithal angle of the GNSS signal path, is the mean earth radius and is the peak height, considered as equal to 450 km for this simplified mapping function.

Given TEC and VTEC observations from the regional networks, a 3D grid over the Brazilian region was constructed in order to update the background model by performing regional tomography. The spatial resolution of the 3D grid was set with 1.5° in latitude and 1.5° in longitude. The vertical resolution of the 3D grid was constructed with distinct step sizes in order to reduce the number of cells and improve the time process. Considering that the F2 layer has the highest variability, which decreases with height, the vertical resolution was set with a 50 km step size in the region between 50 km and 200 km in height, 25 km step size from 200 km up to 550 km, again 50 km step size but from 550 km up to 700 km, and then a 100 km step size from 700 km up to 1000 km, 200 km step size from 1000 km up to 1600 km, 400 step size from 1600 km up to 2000 km, and 500 km stepsize from 2000 km up to 3000 km. A total of 75000 cells were then created to represent a unique 3D grid in the Brazilian region, which covered the longitudes of -91.5°W and 18°W and latitudes of 51.5°S and 22°N. The spatial coverage includes not only the Brazilian areas, but also the South America, in order to increase the geometry of the GNSS signals used in the ionospheric tomography. A temporal resolution of six minutes was also defined, where the electron density was set to be constant within each cell in such time interval, generating 241 grids to represent a given day.

Each cell of the 3D grid has been filled with the initial guess of the electron density given by the background model. MART was applied then to update the electron density in each cell. In fact, when applying the traditional MART algorithm in the proposed area, many cells of the 3D grid remain non-illuminated. To overcome this problem, Prol et al. (2016) used a spatial resolution of 4° in latitude and 4° in longitude. However, this is a low

257 resolution for representing the ionospheric variability in the Brazilian region. In order to use a
258 smaller spatial resolution of 1.5° by 1.5°, and therefore obtain a better representation of the
259 ionospheric variability in Brazil, a small change has been incorporated in the most usual
260 MART algorithm. The updated electron density in cell is calculated with the following
261 expressions:

262 and

263 where is the electron density obtained from iteration , k is varying with a stepsize
264 of 2 due to the VTEC updates, and are the observed TEC and VTEC of the
265 GNSS signal , is the path length of the GNSS signal inside the boundaries that intersect
266 the cell , is the largest path length of the respective signal , the term is
267 equivalent to a scan through each cell of the ionospheric grid that calculates TEC or VTEC
268 from the background and is a weighting parameter that control the convergence of the
269 algorithm. The difference when using VTEC observations is that and are related to
270 the vertical distance, which are represented by and . The same configurations of Prol
271 et al. (2016) were adopted for the MART reconstruction, i.e., we used an iterative process
272 that cycles through all ray paths 70 times and a weighting parameter of =0.2, being both
273 optimal parameters empirically obtained.

274 Following equations (9) and (10), it can be seen that for each GNSS signal, two
275 observations are used. TEC observations are used to update a set of cells corresponding to a
276 slant direction and VTEC observations are used to update a column of cells in the 3D grid.
277 VTEC values are affected by the single-layer mapping error, which seems contradictory to

the main propose of the tomographic algorithm. However, the incorporation of VTEC values does not significantly affect the slant TEC estimative. Taking one cell as example, it will be illuminated by a unique observation of VTEC. On the other hand, in the areas with a good tomographic geometry coverage, many observations in the slant direction will be used to update the electron density, which will make the slant observation the most important in the correspondent cells. Figure 4 shows an example of the residuals obtained with the proposed tomographic method, which confirms the method fits better to the slant TEC than the VTEC. The important contribution of VTEC is therefore when there are few or none slant observations, in the way that the use of both measurements (slant TEC and VTEC) generates a tomographic reconstruction with an increased number of illuminated cells without significantly affecting the slant TEC estimations. Thus, even with a significative lack of GNSS signals for the tomographic reconstruction, it is possible to take the maximum advantage of the GNSS observations.

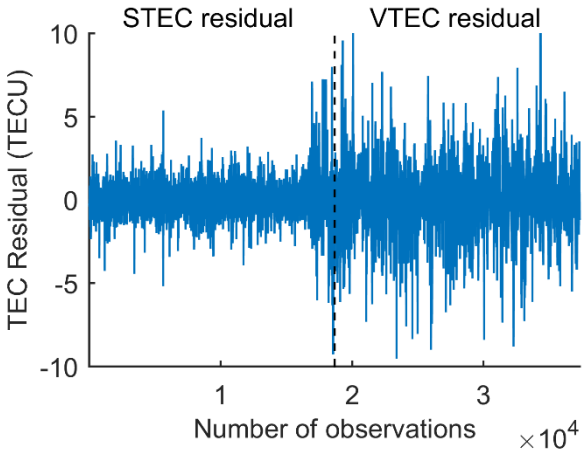

Fig. 4 Slant TEC (STEC) and VTEC residuals obtained with the proposed tomographic algorithm at 18 hours UT in DOY 312 for all GNSS stations.

Figures 5 and 6 shows an example of the tomographic reconstruction of the peak height and the critical frequency when TEC and VTEC observations are used to

298 update the background. The cells without any observation were removed from the
299 tomographic reconstruction, generating the blank spaces on the maps. It is worth mentioning
300 that some artifacts could appear in the reconstruction tomography due to the poor geometry
301 of the GNSS signals. However, no extremely large values of the peak height and critical
302 frequency are obtained, even when looking to results of several days of the tomographic
303 reconstruction, which indicates that the proposed approach is not so susceptible to create
304 artifacts in the reconstructed ionosphere. This can be explained due to the incorporation of
305 VTEC observations that enlarge the number of illuminated cells.

306 In general, a bigger variance is obtained from the reconstruction method, in
307 comparison to the background. This is mainly because the peak height and critical frequency
308 are retrieved considering the vertical resolution of 25 km while the background is obtained by
309 direct interpolation of and measurements. Also, as expected, the peak height
310 estimated with the tomography presented a similar behavior to the background peak height.
311 On the contrary, the critical frequency has presented a reasonable variation at instants with
312 higher values of the electron density. In the example of 02 UT, the tomographic
313 reconstruction has presented the crests of EIA with more intensity. In fact, the tomographic
314 representations at 02 UT seem more realistic than the background because an intensification
315 of the vertical drift is known to occur at such instants (22.5 LT in the central area 50°W),
316 which increases the electron density in the EIA crests. It is typically observed that the upward
317 vertical drift occurs with more intensity in the Brazilian equatorial region in comparison to
318 the other longitudinal sectors. Therefore, considering that the background was obtained
319 gathering global observations in a sun-fixed reference frame, it is expected that the EIA was
320 smoothed at 02 UT in comparison to the tomographic results. On the other hand, at 12 UT
321 and 18 UT, the spatial distribution of EIA in the Brazilian region has similar patterns in
322 comparison with other sectors of the global equatorial ionosphere. Then, it was reasonable to

obtain the spatial distribution of the critical frequency of the background similar to the tomographic solution at 12 UT and 18 UT. Also, higher values of the critical frequency at 18 UT for the tomography are expected because the background is showing a smoothed solution gathering 60 days, while the tomography is updating the background using actual data of DOY 312. Therefore, despite the differences between the background and the tomographic reconstruction, the obtained results presented reasonable justifications, which inspired us to evaluate the quality of the proposed method.

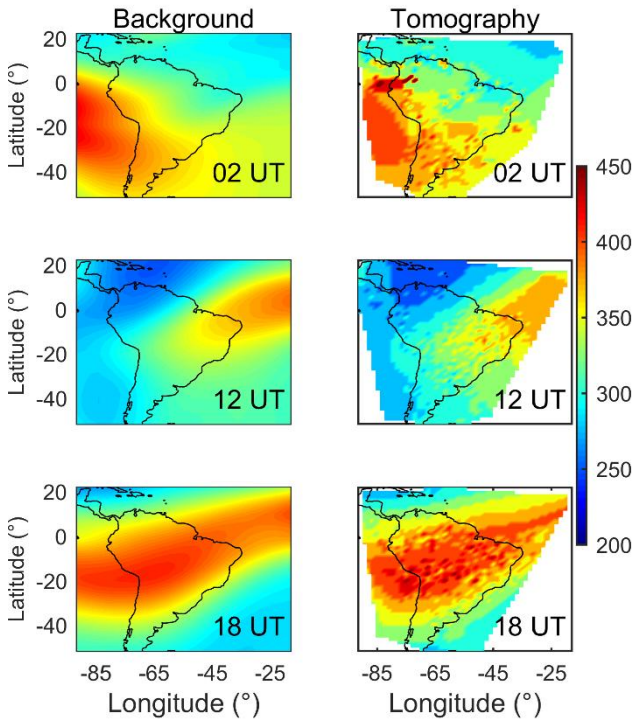

Fig. 5 Peak height maps estimated by the background and the ionospheric tomography for DOY 312 of 2013. The unit of the color bar is in km.

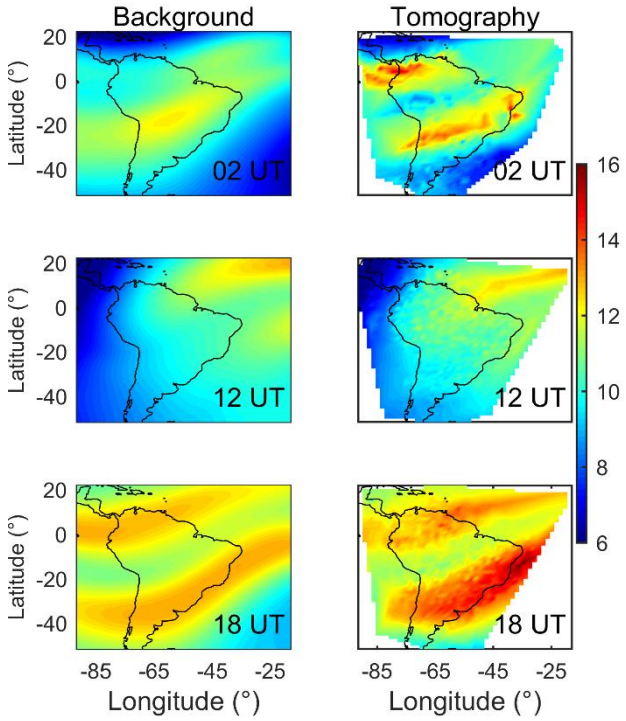

Fig. 6 Critical frequency maps estimated by the background and the ionospheric tomography for DOY 312 of 2013. The unit of the color bar is in MHz.

Assessment of the Height and Electron Density at the Peak

A total of 14 days was selected to evaluate the proposed method during the south hemisphere Summer solstice (hereinafter solstice) and during the south hemisphere Spring equinox (hereinafter equinox) of 2013. The days selected for analysis were DOYs between 229 and 235 for equinox and between 308 and 314 for the solstice. Such DOYs do not coincide exactly with the equinox and solstice, but they were chosen because of the higher amount of data available from the ionosondes installed in Brazil that were scaled manually. At least, three Brazilian ionosondes had available data for the chosen DOYs. Also, the year of 2013, which was close to the maximum in the solar cycle 24, was selected in order to evaluate the method in an epoch with high ionospheric variability but with no intense scintillations.

Figure 7 shows the values of and estimated by the proposed method, IRI-2012 and observed by the SAA0K ionosonde. Indeed, the SAA0K measurements were not used in the background modeling neither in the tomography, which makes the validation reliable. It can be seen that the tomographic and IRI results show a similar daily behavior in comparison to the reference values. The magnitude of the estimated and observed values of is varying between 3 MHz and 13 MHz in the equinox, with an increasing during the solstice and reaching a maximum near 16 MHz. The magnitude of the estimated and observed values of is varying between 200 km and 450 km in the equinox, with an increasing during the solstice and reaching a maximum near 550 km. In general, a slight better performance can be visually seen by the tomographic method in comparison to IRI for both and , which is more evident in the solstice and mainly during the daytime. After the daytime, specifically during the transition from the daytime to the nighttime, a peak of and is observed from the ionosonde and even better estimated by the tomographic algorithm. At such instants, the resultant force of the electric field intensifies the vertical drift of the ionosphere upwards, increasing the peak height and displacing the plasma to higher altitudes, in the way that the proposed method was capable of showing the ionospheric enhancement called as the pre-reversal period.

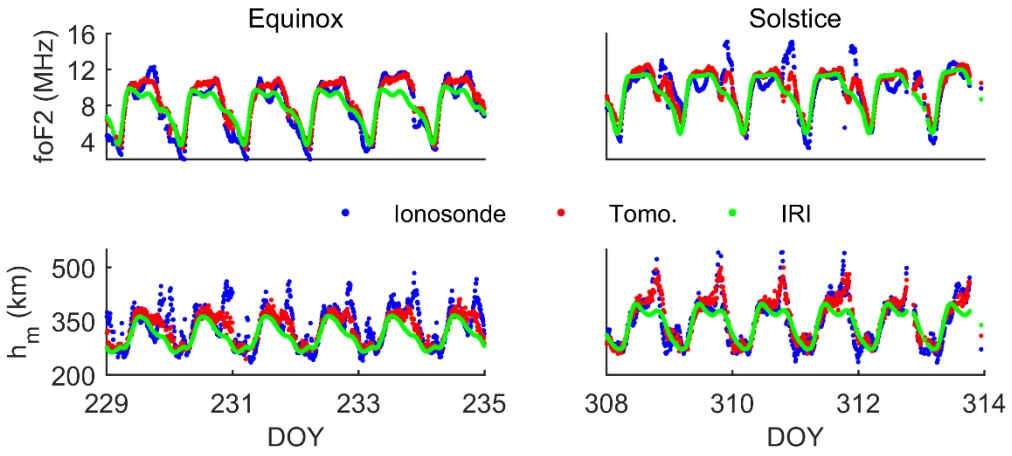

Fig. 7 Critical frequency and peak height observed in ionosonde SAA0K and estimated with IRI-2012 and the tomographic method (Tomo.).

Figure 8 shows the absolute error of the estimated values of and and also the average of the errors (colored lines) in terms of LT. Despite BVJ03 and FZA0M data are used in the background modelling, we can see a similar magnitude of the error when comparing BVJ03 and FZA0M data with the independent data of SAA0K station. This is important because it shows that no constraints have been incorporated to fix the ionosonde observations in the proposed method, which means that RO and GNSS data also played an important role to the estimation of the ionosphere in the location of the ionosondes. In terms of the daily variation, the larger errors are noticed between 18 and 24 LT, as expected, because it is coincident with the pre-reversal enhancement of the ionospheric vertical plasma drift. In addition, it can be seen a larger maximum error for IRI, reaching up to 6 MHz for and 200 km for , as well as a smaller average error of the proposed method given by the red lines.

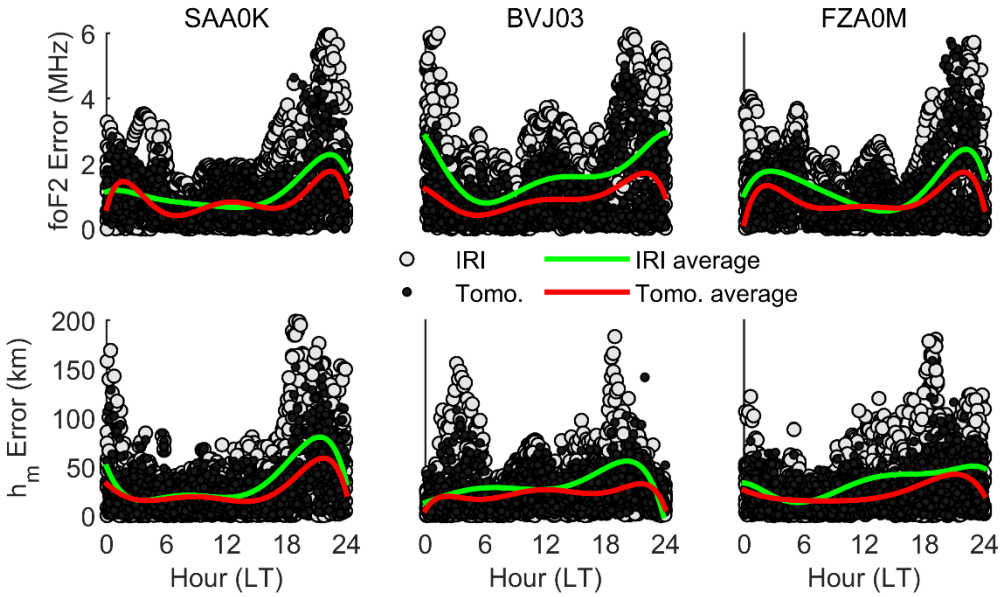

Fig. 8 The absolute error of the critical frequency and peak height obtained with IRI and the tomographic reconstruction (dots) and average of the absolute errors (colored lines).

Table 1 shows the RMSE (Root Mean Square Error) for all ionosondes in the equinox and solstice. The total RMSE obtained in the equinox was 0.85 MHz ( ) and 32.07 km ( ) for the proposed method and 1.35 MHz ( ) and 47.34 km ( ) for IRI. Also, the total RMSE in the solstice was 1.54 MHz ( ) and 31.45 km ( ) for the proposed method and 2.10 MHz ( ) and 43.87 km ( ) for IRI. This indicates that the tomographic reconstruction presented an improvement in the equinox of 37% for and 32% for . At the solstice, the improvement seems to be a bit lower, but also significative, achieving 26% for and 28% for . The improvement is quite similar, but a bit lower, when looking only to the independent data of the SAA0K station (in bold), reaching 26% ( ) and 29% ( ) in the equinox and 22% ( ) and 33% ( ) in the solstice.

Table 1 – RMSE of and for the analyzed Equinoxes and Solstices periods. Units of in MHz and units of in km.

Station	Equinox Tomo. //	Equinox IRI //	Solstice Tomo. //	Solstice IRI //
SAA0K	**1.02 // 38.53**	**1.36 // 53.94**	**1.31 // 29.52**	**1.68 // 44.17**
BVJ03	0.62 // 28.27	1.29 // 45.69	1.71 // 29.02	2.50 // 37.47
FZA0M	0.87 // 28.30	1.39 // 41.55	1.58 // 35.42	2.03 // 49.20
All	0.85 // 32.07	1.35 // 47.34	1.54 // 31.45	2.10 // 43.87

Based on the results of the entire section, it can be said that the proposed method better estimated the ionosphere at the analyzed ionosondes in many aspects when compared to the IRI solutions. In addition to the statistical improvements, the main important improvement of the proposed method was the peak height estimation at the post-sunset pre-reversal period. The strong vertical drift upwards during the pre-reversal peak is an important event in the Brazilian region that, as it can be noticed, is not represented by IRI. The

409 proposed method, therefore, can be a useful tool for several studies related with the pre-
410 reversal enhancement of the F-region vertical drift, which has been a continuous challenge to
411 analyze with empirical models. In fact, the general daily variation of the ionosphere seems to
412 be better represented by the tomography. Despite IRI is a climatological model, such
413 improvements and representations are not so easily obtained by regional methods. For
414 instance, previous works using tomographic reconstruction in Brazil (Prol et al. 2016) have
415 also presented a better estimation of . However, it was overestimated in the nighttime due
416 to problems with mapping the topside coupled to the fact that the background was directly
417 derived from IRI. Now, the background is based on actual data and using a new formulation
418 for the topside, which played an important role in the obtained results. Prol et al. (2016) also
419 found problems in mapping the ionosphere at the edge of the 3D grid. At that time, the
420 ionosonde located in Fortaleza (FZA0M) presented a lower performance in comparison to
421 IRI. But now, the geometry of the reconstruction was not so problematic in the edges of the
422 grid due to the better background modelling and the use of VTEC together with the
423 tomography.
424
425 **Assessment of TEC and PPP**
426 The TEC and single-frequency PPP assessment has been performed using the same
427 tomographic results of the previous sections and covering the same two weeks of data during
428 the equinox and solstice of 2013. The main point here was to evaluate the quality of the
429 proposed method in terms of the ionospheric delay. Therefore, an evaluation has been made
430 to check the quality of the tomographic reconstruction compared with results derived from
431 most usual products for GNSS applications, i.e., the GIMs provided by IGS. The UQRG
432 GIMs were selected for the comparison because it has shown better results in particular for
433 the low-latitude ionosphere in comparison to other GIMs (see for instance Orús et al. 2016)

434 and also due to the temporal resolution of 15 minutes, while other products from IGS have a
435 temporal resolution of one or two hours.

436 Figure 9 shows histograms of the TEC error calculated for the analyzed two weeks
437 and six GNSS stations not included in the tomographic reconstruction, where the reference
438 values of TEC were obtained in the slant direction using the calibration procedure presented
439 in equations (5) and (7). In general, both ionospheric models presented the TEC error
440 centered at zero, which means that both methods provided an unbiased solution. Also, most
441 of the TEC errors appear between -10 TEC Units (TECU, being 1 TECU=10^{16} el/m²) and 10
442 TECU, showing a similar good performance of both models. However, the TEC error close to
443 zero is observed more often for the tomographic reconstruction. The frequency of the TEC
444 errors closer to zero is sometimes twice for the tomography, indicating a clear better solution,
445 except in the SPCA observatory, which the improvement was not so evident. Indeed, SPCA
446 station is located in the region with the highest variability of TEC, so it is reasonable that this
447 was the most difficult region to map in the south crest of the EIA. Despite not being so
448 evident in the histogram, the RMSE of SPCA given in Table 2 shows a clear better
449 performance for the tomographic method. The RMSE in SPCA was 1.72 TECU for the
450 tomographic method and 4.88 TECU for the UQRG GIM, showing an improvement of 64%.
451 Also in terms of the RMSE, the worst TEC error of the tomography is observed for the site of
452 BRAZ. This occurred because the closest station from BRAZ during the equinox was about
453 300 km far when performing the tomographic reconstruction. Thus, the ionospheric mapping
454 over the BRAZ station was considered a difficult task. However, when looking for the error
455 of all stations, the RMSE was 1.88 TECU for the tomographic method and 4.59 TECU for
456 the UQRG GIM, which show a general improvement of 59%.
457

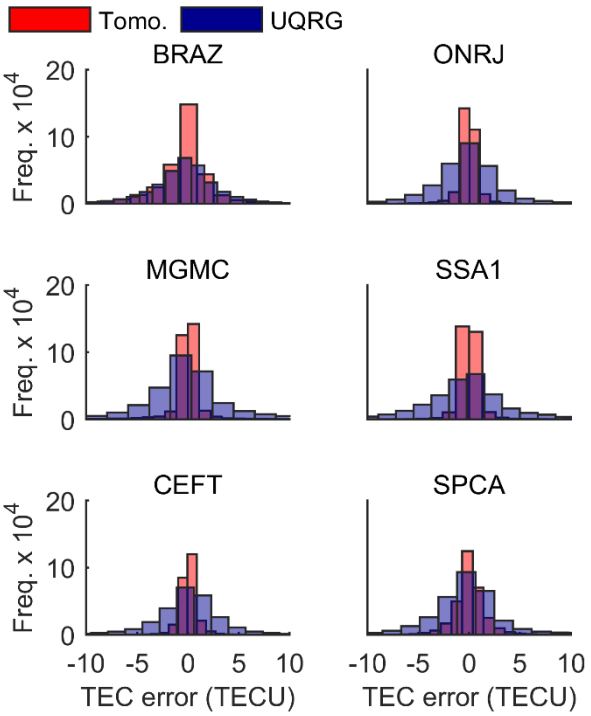

Fig. 9 Set of histograms showing the frequency (Freq.) of the TEC errors during the analyzed two weeks using the tomographic method (Tomo.) and the UQRG maps.

Table 2 – TEC RMSE obtained with the UQRG GIM and the tomographic reconstruction method. Units in TECU.

Station	Tomography	UQRG GIM
BRAZ	3.03	3.97
ONRJ	1.51	4.35
MGMC	1.96	5.01
SSA1	1.28	5.39
CEFT	1.10	3.72
SPCA	1.72	4.88
All	1.88	4.59

In order to analyze the performance of TEC as applied to the GNSS positioning, some adaptations have been implemented in RTKLib (Takasu and Yasuda, 2009) for the calculation of the ionospheric delay based on 3D grids. As far as the authors have found, this is the first time that three-dimensional grids with high resolution are directly applied at low latitudes in the single-frequency GNSS positioning without the need of mapping functions to convert VTEC into the slant direction, where the main goal here was devoted to the use of

GNSS positioning techniques to assess the quality of the TEC retrieved from the tomographic method. In this regard, the single-frequency PPP in the kinematic mode has been chosen for the quality checking. The kinematic single-frequency PPP direct applies the modeled ionospheric delay to correct the GNSS observation epoch by epoch. Therefore, it seems a good option to provide a straightforward information about the performance of the ionospheric model, also because the majority of other effects are mitigated, such as the tropospheric refraction, earth tides and others.

In general, three modes of PPP are analyzed: (a) using the ion-free observation (PPP/ionf); (b) using L1 and ionospheric delay from UQRG GIMs (PPP/uqrg); and (c) using L1 and TEC estimated through the tomographic method (PPP/tomo). Among the PPP configurations, we used the following: (1) combined solution obtained by forward and backward filters; (2) cut-off angle of 10°; (3) earth tides corrections; (4) estimation of tropospheric delay during PPP; (5) precise ephemerides (sp3) and satellite clock corrections (clk_30s) acquired from IGS products; (6) only GPS constellation; (7) correction of the Phase Center Variation (PCV) of the antenna; (8) phase wind up corrections; (9) no strategy for ambiguity solution; and (10) corrections of the differential instrumental bias between the civil and precise codes (C1-P1) when P1 was not available.

Figure 10 shows the 3D errors of PPP/ionf, PPP/uqrg and PPP/tomo during the equinox. The 3D error was computed by taking the RMSE of all solutions in terms of LT. The reference coordinates were obtained from the final solution of SIRGAS (SIstema de Referencia Geocéntrico para las AméricaS), at epoch 2013, and a time update was performed to make the reference coordinates consistent with the epoch of the PPP solutions. The good results of the ionfree indicate that almost all errors were efficiently mitigated. Also, the PPP/tomo solution was close to the ionfree in the beginning of the day for almost all stations, showing that the PPP/tomo algorithm was capable to mitigate several errors. The remaining

errors, therefore, were mainly related to the accuracy of TEC retrieved from the tomographic model. In this respect, it is expected a worsening of the PPP/tomo accuracy during the daytime and near 15 LT due to the daily variability of the ionosphere. Despite a lower accuracy of PPP/tomo during the daytime, even at such times, a better performance of PPP/tomo was obtained in comparison to PPP/uqrg for almost all stations. Only in the BRAZ station that PPP/uqrg performed better. Indeed, when looking for the location of the stations used in the ionospheric tomography, the closest station to BRAZ was more than 300 km far. So, it is difficult to represent the ionospheric variability in the region near the BRAZ with the tomographic reconstruction. In addition, the UQRG maps were obtained using the BRAZ observations, enhancing its better accuracy to describe the ionosphere in the region.

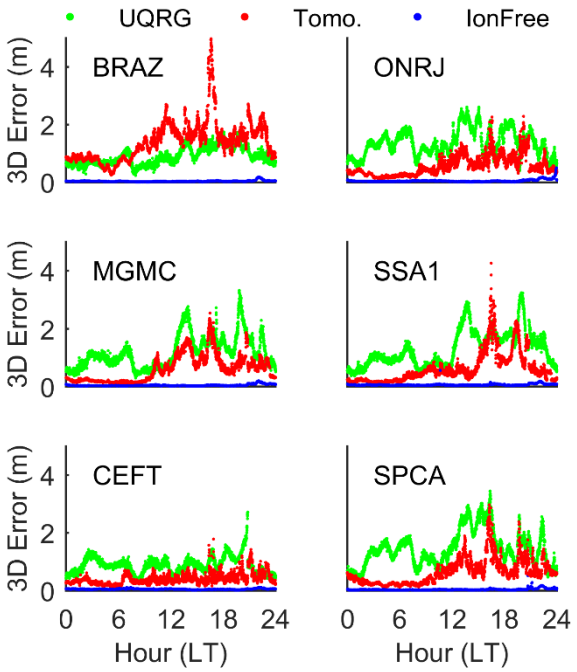

Fig. 10 RMSE of the three-dimensional error for all analyzed stations in the equinox of 2013.

Figure 11 shows the 3D errors, giving in terms of RMSE and LT, of PPP/ionf, PPP/uqrg and PPP/tomo during the solstice of 2013. Now, the PPP/tomo solution presented a better performance in comparison to PPP/uqrg for all stations. PPP/tomo presented an even

513 better accuracy in the BRAZ station. Indeed, now the closest station from BRAZ was ~100
514 km far, improving the representation of the ionospheric variability around the region. In
515 comparison to the equinox, a general worst performance was obtained for all PPP methods
516 due to the higher values of TEC in the solstice. In addition, the most significative errors are
517 noticed after 18 LT, when the ionospheric irregularities were more effective to impact the
518 GPS observations. At such instants, the uplifted ionosphere generates high vertical gradients
519 due to the pre-reversal drift. It is believed that these gradients set the preconditions for a
520 plasma instability, which controls the generation of ionospheric irregularities driven by the
521 gravitational Rayleigh–Taylor mechanism. The change of the GPS phase observations
522 imposed by the ionospheric irregularity results in the amplitude and phase scintillation, which
523 degrades the PPP solution. Therefore, the ionospheric irregularities causing scintillations
524 were the main cause of the worst results of PPP/uqrg, PPP/tomo and PPP/ionf during the
525 solstice. It is interesting to notice that even with the elimination of the first-order ionospheric
526 delay in PPP/ionf, it was not enough to mitigate the scintillation impact in the GPS signals.
527

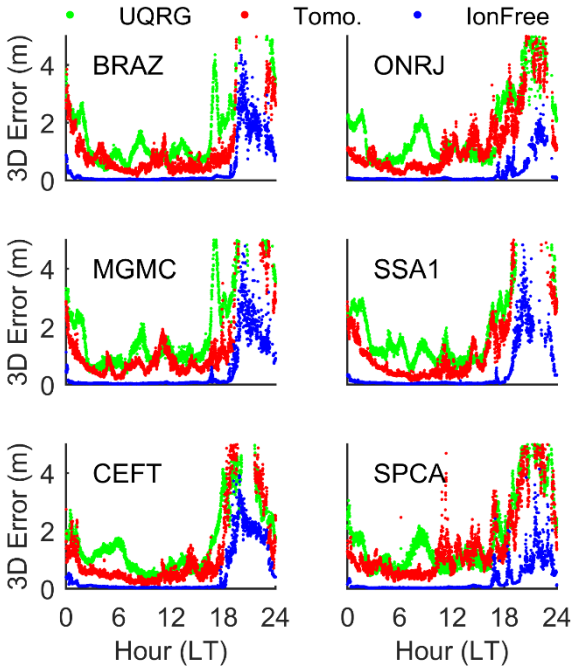

528

529 **Fig. 11** RMSE of the three-dimensional error for all analyzed stations in the solstice of 2013.

Table 3 shows the total RMSE obtained for each station, where the data with scintillations were excluded from the statistics. The differences between the equinox and solstice are not so evident, except for the PPP/tomo and the station BRAZ due to the already mentioned lack of data during the equinox. When looking at the general results, while the ionfree solution remains within a centimeter accuracy around 0.05 m, we can see that the PPP/tomo solution presented a decimeter accuracy around 0.83 m and that the PPP/uqrg showed a metric accuracy around 1.21 m. The total improvement of PPP/tomo in comparison to the PPP/uqrg is about 31%, which indicates that the proposed method seems to be efficient to represent the ionospheric delay with enough accuracy to improve the GNSS positioning in comparison to one of the most traditional methods.

Table 3 – RMSE of PPP for the equinox and Summer solstice of 2013. Units in meters and hours with scintillations were excluded.

Station	PPP/ionf Equinox // Solstice	PPP/tomo Equinox // Solstice	PPP/uqrg Equinox // Solstice
BRAZ	0.04 // 0.05	1.57 // 0.63	0.95 // 1.03
ONRJ	0.06 // 0.04	0.65 // 0.80	1.44 // 1.16
MGMC	0.05 // 0.05	0.75 // 0.72	1.31 // 1.12
SSA1	0.06 // 0.05	0.80 // 0.69	1.41 // 1.31
CEFT	0.05 // 0.07	0.45 // 0.58	0.93 // 1.01
SPCA	0.05 // 0.05	0.77 // 1.01	1.57 // 1.06
All	0.05 // 0.05	0.92 // 0.75	1.30 // 1.12

Conclusions

A new tomographic algorithm was successfully implemented and assessed in the Brazilian region. The performance of the proposed method was evaluated for the estimation of , and TEC and a pioneering application checked the performance of the tomographic algorithm when used to correct the single-frequency PPP. The experimental results using independent ionosonde data as reference presented an improvement of about 24% for and 31% for in comparison to IRI-2012. In terms of the ionospheric delay,

the tomographic reconstruction showed an improvement of 59% for TEC and 31% for the single-frequency PPP when compared with the one corrected with the UQRG GIM in six GNSS stations that were not used in the tomography. This indicates that the proposed method seems efficient to represent the ionospheric morphology given by , and TEC at the Brazilian region and also to estimate the ionospheric delay with enough accuracy to improve the GNSS positioning in comparison to the conventional methods. Therefore, it can be considered a useful tool for several applications of Space Weather, Telecommunications and Spatial Geodesy in the Brazilian region.

Another relevant finding is that the proposed method was capable of showing the upward vertical drifts associated with the post-sunset electric field pre-reversal enhancement, which has been a continuous challenge for empirical methods. At such instants, the uplifted ionosphere is probably the main reason for the generation of ionospheric irregularities, which results in amplitude and phase scintillations. Despite the ionospheric tomography is capable of showing the ionospheric vertical drift, the PPP solution has been significantly affected during the pre-reversal enhancement. However, no vertical information of the ionosphere is used together with the ionospheric delay to mitigate the scintillations. It is therefore suggested to check the possibility of using the vertical information given by the proposed method to predict the impact of ionospheric irregularities in GNSS signals. Then, would be relevant to check if this information could improve the accuracy of the single-frequency PPP even during the most challenge conditions of ionospheric scintillations.

Acknowledgements

This work was jointly funded by Coordenação de Aperfeiçoamento de Pessoal de Nível Superior (CAPES), Fundação de Amparo à Pesquisa do Estado de São Paulo (FAPESP Grants: 2015/15027-7 and 2016/22011-2) and Conselho Nacional de Desenvolvimento Científico e Tecnológico (CNPq Grants: 304674/2014-1 and 429885/2016-4). The authors

578 are grateful to UCAR (USA) and NSPO (Taiwan) for providing FORMOSAT-3/COSMIC
579 RO data, to IGS, RBMC, LISN, CALIBRA and RAMSAC for providing GNSS data and to
580 the IRI model developers due to its usage in the electron density analysis.

581

582 **References**

583 Abdu, M. A. A., E. R. de Paula, I. S. Batista, B. W. Reinisch, M. Matsuoka, P. Camargo, O.
584 Veliz, C. M. Denardini, J. H. A. Sobral, E. A. Kherani, and P. Sequeira (2008) Abnormal
585 evening vertical plasma drift and effects on ESF and EIA over Brazil-South Atlantic sector
586 during the October 30, 2003 super-storm, J. Geophys. Res., 113(A7), A07313

587 Aguiar, C. R.; Camargo, P. O. (2012) Resolução espacial da grade ionosférica e do GIVE.
588 Bol. Cienc. Geod. 18(3):464-479

589 Austen JR, Franke SJ, Liu CH (1988) Ionospheric imaging using computerized tomography.
590 Radio Sci 23:299–307

591 Batista, I.S., Medeiros, R.T., Abdu, M.A., de Souza, J.R., Bailey, G.J., de Paula, E.R., 1996.
592 Equatorial ionospheric vertical plasma drift model for the Brazilian region. J. Geophys.
593 Res. 101, 10887–10892

594 Batista IS, Abdu MA, Carrasco AJ, Reinisch BW, de Paula ER, Schuch NJ, Bertoni F (2008)
595 Equatorial spread F and sporadic E-layer connections during the Brazilian Conjugate Point
596 Equatorial Experiment (COPEX). J Atmos Sol Terr Phys 70:1133–1143

597 Bilitza D., D. Altadill, Y. Zhang, C. Mertens, V. Truhlik, P. Richards, L.-A. McKinnell, and
598 B. Reinisch (2014) The International Reference Ionosphere 2012 – a model of
599 international collaboration, J. Space Weather Space Climate, 4[A07], 1-12

600 Bust GS, Mitchell CN (2008) History, current state, and future directions of ionospheric
601 imaging. Rev Geophys 46:RG1003

602 Camargo PO, Monico JFG, Ferreira LDD (2000) Application of ionospheric corrections in
603 the equatorial region for L1 GPS users. Earth Planets Space 52(11): 1083–1089

604 Ely CV, Batista IS, Abdu MA (2012) Radio occultation electron density profiles from the
605 FORMOSAT-3/COSMIC satellites over the Brazilian region: a comparison with
606 Digisonde data. Adv Space Res 49(11):1553–1562

607 Ghaffari Razin M. R., Voosoghi, B. (2017) Ionosphere tomography using wavelet neural
608 network and particle swarm optimization training algorithm in Iranian case study. GPS
609 Solut. 21:1301-1314

610 Haase JS, Dautermann T, Taylor MJ, Chapagain N, Calais E, Pautet D (2011) Propagation of
611 plasma bubbles observed in Brazil from GPS and airglow data. Adv Space Res 47:1758–
612 1776

613 Hernández-Pajares, M., Juan, J. M., Sanz, J., & Solé, J. G. (1998). Global observation of the
614 ionospheric electronic response to solar events using ground and LEO GPS data. Journal
615 of Geophysical Research: Space Physics, 103(A9), 20789-20796.

616 Hernández-Pajares, M., Juan, J. M., and Sanz, J. (1999). New approaches in global
617 ionospheric determination using ground GPS data. Journal of Atmospheric and Solar-
618 Terrestrial Physics 61, 1237–1247

619 Hernández-Pajares, M., M. Garcia-Fernàndez, A. Rius, R. Notarpietro, A. von Engeln, G.
620 Olivares-Pulido, À. Aragón-Àngel, and A. García-Rigo (2017), Electron density
621 extrapolation above F2 peak by the linear Vary-Chap model supporting new Global
622 Navigation Satellite Systems-LEO occultation missions, J. Geophys. Res. Space Physics,
623 122, doi:10.1002/2017JA023876.

624 Howe BM, Runciman K and Secan JA. 1998. Tomography of the ionosphere: Four-
625 dimensional simulations. Radio Sci 33(1): 109-128.

626 Kunitsyn V, Nesterov I, Padokhin A, Tumanova Y (2011) Ionospheric Radio Tomography
627 Based on the GPS/GLONASS Navigation Systems. Journal of Communications
628 Technology and Electronics. 56(11): 1269-1281

629 Machado W.C., Fonseca Jr E.S (2013) Artificial neural networks applied to VTEC prediction
630 in Brazil. Bol. Cienc. Geod. 19(2):227–246

631 Materassi M, Mitchell CN (2005) Imaging of the equatorial ionosphere. Ann Geophys
632 48(3):477–482

633 Mitchell CN and Spencer PS. 2003. A threedimensional time-dependent algorithm for
634 ionospheric imaging using GPS. Ann Geophys 46(4): 687-696

635 Muella MTAH, de Paula ER, Mitchell CN, Kintner PM, Paes RR, Batista IS (2011)
636 Tomographic imaging of the equatorial and low-latitude ionosphere over central-eastern
637 Brazil. Earth Planets Space 63:129–138

638 Olivares-Pulido, G., M. Hernández-Pajares, A. Aragón-Angel, and A. Garcia-Rigo (2016), A
639 linear scale height Chapman model supported by GNSS occultation measurements, J.
640 Geophys. Res. Space Physics, 121.

641 Orus, R. (2015), Ionospheric error contribution to GNSS single-frequency navigation at the
642 2014 solar maximum, Journal of Geodesy DOI 10.1007/s00190-016-0971-0

643 Prol FS and Camargo PO (2016) Ionospheric tomography using GNSS: multiplicative
644 algebraic reconstruction technique applied to the area of Brazil. GPS Solut. 20(4): 807-
645 814.

646 Prol, F. S.; Camargo, P. O.; Muella, M. T. A. H. (2017) Numerical Simulations to Assess
647 ART and MART Performance for Ionospheric Tomography of Chapman Profiles. An.
648 Acad. Bras. Ciênc., 89:1531-1542

649 Prol FS.; Camargo PO; Monico JFG; Muella MTAH (2018) Assessment of a TEC calibration
650 procedure by single frequency PPP. GPS Solut., Online First, doi: 10.1007/s10291-018-
651 0701-6

652 Pryse SE, Kersley L, Mitchell CN, Spencer PSJ, Williams MJ (1998) A comparison of
653 reconstruction techniques used in ionospheric tomography. Radio Sci 33(6):1767–1779

654 Raymund Td, Franke Sj And Yeh KC. 1994. Ionospheric tomography: its limitations and
655 reconstruction methods. J Atmos Sol-Terr Phys 56(5): 637-655

656 Ramakrishnan, S.; K. Rawer. (1972) Model electron density profiles obtained by empirical
657 procedures. In: Space Research XII, Akademie-Verlag, Berlin, p. 1253-1261

658 Rishbeth H (2000) The equatorial F-layer: progress and puzzles. Ann Geophys 18:730–739

659 Seemala GK, Yamamoto M, Saito A and Chen CH. 2014. Three- dimensional GPS
660 ionospheric tomography over Japan using constrained least squares. J Geophys Res
661 119(4): 3044-3052

662 She C., Wan W., Yue X., Xiong B., Yu Y., Ding F., Zhao B. (2017) Global ionospheric
663 electron density estimation based on multisource TEC data assimilation. GPS Solut.
664 21(3):1125-1137

665 Takasu T, Yasuda A (2009) Development of the low-cost RTK-GPS receiver with an open
666 source program package RTKLIB. International symposium on GPS/GNSS, Seogwipo-si
667 Jungmun-dong, Korea, 4–6 November

668 Tulasi Ram S, Su SY, Liu CH (2009) FORMOSAT-3/COSMIC observations of seasonal and
669 longitudinal variations of equatorial ionization anomaly and its interhemispheric
670 asymmetry during the solar minimum period. J Geophys Res 114:A06311

671 Wen DB, Wang Y, Norman R (2012) A new two-step algorithm for ionospheric tomography
672 solution. GPS Solut 16(1):89–94

673 Yao YB, Chen P, Zhang S, Chen JJ (2013) A new ionospheric tomography model combining
674 pixel-based and function-based models. Adv Space Res 52:614–621

675 Yin, P., Zheng, Y. N., Mitchell, C. N. and Li, B., 2017. A multiresolution inversion for
676 imaging the ionosphere. Journal of Geophysical Research: Space Physics 122(6):6799-
677 6811

678 Zhao B, Wan W, Yue X, Liu L, Ren Z, He M, Liu J (2011) Global characteristics of
679 occurrence of an additional layer in the ionosphere observed by COSMIC/FORMOSAT-3.
680 Geophys Res Lett 38:L02101

681 Zheng, D., Hu, W., Nie, W., 2015. Multiscale ionospheric tomography. GPS Solut. 19 (4),
682 579–588

683